PCCP

PAPER

View Article Online
View Journal

Micellar drug nanocarriers and biomembranes: how do they interact?†‡

Cite this: DOI: 10.1039/c3cp54242d

Antonio De Nicola,[ab] Samira Hezaveh,[c] Ying Zhao,[d] Toshihiro Kawakatsu,[e] Danilo Roccatano[c] and Giuseppe Milano*[ab]

Received 8th October 2013,
Accepted 3rd January 2014

DOI: 10.1039/c3cp54242d

www.rsc.org/pccp

Pluronic based formulations are among the most successful nanomedicines and block-copolymer micelles including drugs that are undergoing phase I/II studies as anticancer agents. Using coarse-grained models, molecular dynamics simulations of large-scale systems, modeling Pluronic micelles interacting with DPPC lipid bilayers, on the μs timescale have been performed. Simulations show, in agreement with experiments, the release of Pluronic chains from the micelle to the bilayer. This release changes the size of the micelle. Moreover, the presence of drug molecules inside the core of the micelle has a strong influence on this process. The picture emerging from the simulations is that the micelle stability is a result of an interplay of drug–micelle core and block-copolymer–bilayer interactions. The equilibrium size of the drug vector shows a strong dependency on the hydrophobicity of the drug molecules embedded in the core of the micelle. In particular, the radius of the micelle shows an abrupt increase in a very narrow range of drug molecule hydrophobicity.

Introduction

In medicine the use of nanosized tools for the diagnosis, prevention and treatment of diseases is becoming more and more popular.[1] First generation nanomedicines, nowadays, are in routine clinical use and include both ''blockbuster'' drugs and certain specific products.[2] In this context the use of polymeric materials is very broad[3] and polymer based formulations are among the most successful nanomedicines.[3–7]

Among several diseases, cancer is a major target of the development of new drugs with many clinical trials ongoing and involving nanomedicines.[8] Technologies include liposomes,[9–11] polymer conjugates[3–5] and block copolymer micelles.[6,7,12,13] Tumor angiogenesis creates the gateway for nanosized objects to access tumors. Matsumura and Maeda described the enhanced permeability and retention (EPR) effect in the 1980s,[14] the ''gaps'' created by angiogenesis can be much larger (100 nm to 2 μm) than those reported in normal tissues. For this main reason, nanosized drugs tend to accumulate in tumor tissues much more than they do in normal tissues. Due to the EPR effect, for these drug vectors, it is clear that the size of the drug carrier plays an important role. In fact, constructs in the size range of 5–30 nm are considered optimal, and thus the control of the size of systems for drug delivery is a key point.

Block copolymer micelles including drugs by physical entrapment are undergoing phase I/II studies as anticancer agents.[1] Pluronics as micellar aggregates have been employed to store several drugs,[15–18] where Pluronics are amphiphilic linear triblock copolymers having the central block of hydrophobic polypropylene oxide (PPO) covalently bonded with two blocks of hydrophilic polyethylene oxide (PEO). One example of successful application of Pluronics is the doxorubicin formulation SP1049C developed using a combination of two Pluronics, L61 and F127.[19]

Despite the large interest in Pluronic block copolymers for cancer therapy, only recently they became the subject of molecular simulation studies involving biomembranes.[20–25] The understanding of the interaction mechanisms of these synthetic polymers with biomembranes would need a description at the atomic level of both structure and dynamics of the systems. Atomistic models can provide very accurate descriptions by using suitable force fields and they are potentially able to give consistent information. Such a kind of model suitable for Pluronics has been proposed and validated in water and several solvents.[26–28] These models have been used to study the percolation and distribution of PEO chains using steered molecular dynamics, PEO and PPO oligomers[20,23] and Pluronics inside model biomembranes.[21,22] So far, none of these simulation

[a] Dipartimento di Chimica e Biologia, Università di Salerno, I-84984 via Ponte don Melillo, Fisciano (SA), Italy. E-mail: gmilano@unisa.it
[b] IMAST Scarl-Technological District in Polymer and Composite Engineering, P.le Bovio 22, 80133 Napoli (NA), Italy
[c] Jacobs University Bremen, Campus Ring 1, D-28759 Bremen, Germany
[d] Institute of Nano-photonics, School of Physics and Material Engineering, Dalian Nationalities University, Dalian 116600, China
[e] Department of Physics, Tohoku University, Aoba, Aoba-ku, Sendai 980-8578, Japan

† Dedicated to the 80th birthday of Prof. Adolfo Zambelli.

‡ Electronic supplementary information (ESI) available. See DOI: 10.1039/c3cp54242d

studies have been addressed to understand the mechanism of interaction of Pluronic self-assembled structures like micelles with models of cell membranes. These studies are difficult because they involve the simulation of systems on length and time scales not accessible by atomistic simulation methods. To this end, specific coarse-grained models that are able to keep molecular specificity can be used in order to reach time and length scales relevant to these systems. The dynamics of these processes, at molecular level, is so fast that also the experimental measurements cannot easily accessible, and therefore many questions are still undisclosed on the molecular details of the interaction mechanisms.

In this paper, we report the development and validation of coarse-grained models of Pluronics that are able to describe micellar assemblies and their interactions with phospholipids. Furthermore, we employ these models for large-scale simulations of Pluronic L64 micelles interacting with dipalmitoylphosphatidylcholine (DPPC) lipid bilayers. Due to the relevance of these block-copolymers, assembled nanostructures for drug delivery applications, the role of embedded drug molecules has also been considered. In particular, we focused on the interplay of the interactions of drug molecules with the hydrophobic core of the micelle and their mutual influence on the micelle stability in the presence of lipid bilayer structures.

Models and method

Simulation methodology

The coarse-grained (CG) models considered in this work have been developed in a hybrid particle–field (PF) scheme combining particles with a field representation for non-bonded interactions.

Hybrid models, due to their computational efficiency, are gaining popularity for simulations of several soft matter systems including nanocomposites[29] and biomembranes.[30,31] For example, a solvent-free coarse-grained model for lipid bilayer membranes where nonbonded interactions were treated with a weighted-density functional has been introduced by Hömberg and Müller.[32] Very recently, Sevink *et al.*[33] introduced a hybrid scheme, combining Brownian dynamics (BD) and dynamic density functional theory (DDFT), that is able to model efficiently complete vesicles with molecular detail.

Particle and field representation of coarse-grained models has been considered in the single chain in mean field (SCMF) method and has been applied to homopolymer and block copolymer systems as reported by Muller *et al.*[34,35] More recently, the Molecular Dynamics (MD) method has been combined with self-consistent field (SCF) description, which hereafter we call the ''MD-SCF'' approach. In particular, an implementation suitable for the treatment of atomistic force fields and/or specific CG models has been reported and validated.[36,37]

The main feature of the MD-SCF approach is that the evaluation of non-bonded forces and the potential between atoms of different molecules is replaced by the evaluation of a potential dependent on the local density at position **r**. According to SCF theory, a many body problem like molecular motion in a many-molecule system is reduced to the derivation of a partition function of a single molecule in an external potential $V(\mathbf{r})$. Then, forces between non-bonded particles can be obtained from a suitable expression of the $V(\mathbf{r})$ and its derivatives.

In the framework of SCF theory, a molecule is considered to be interacting with the neighbouring molecules only through a mean field. To derive such a mean-field picture, we split the Hamiltonian of our target system, composed of M molecules, into two parts:

$$\hat{H}(\Gamma) = \hat{H}_0(\Gamma) + \hat{W}(\Gamma), \tag{1}$$

where Γ specifies a point in the phase space, which is used as shorthand for a set of positions of all atoms in the system. Moreover, we denote with the symbol ^ (hat) that the associated physical quantity is a function of the microscopic states described by the phase space Γ.

The term $\hat{H}_0(\Gamma)$ is the Hamiltonian of a reference system composed of non-interacting molecules including all the intramolecular interaction terms (bond, angle, *etc.*) that are usually considered in MD simulations. The term $\hat{W}(\Gamma)$ is the deviation from the reference system due to non-bonded interactions.

The partition function of the system, assuming the canonical (NVT) ensemble, is given by:

$$Z = \frac{1}{M!}\int \mathrm{d}\Gamma \exp\{-\beta[\hat{H}_0(\Gamma) + \hat{W}(\Gamma)]\}, \tag{2}$$

where:

$$\beta = \frac{1}{k_B T}$$

From a microscopic point of view, the number density of segments can be defined as a sum of delta functions placed at the center of mass of each particle as:[36]

$$\hat{\phi}(\mathbf{r};\Gamma) = \sum_{p=1}^{M}\sum_{i=0}^{S(p)} \delta\left(\mathbf{r} - \mathbf{r}_i^{(p)}\right), \tag{3}$$

where $S(p)$ is the number of particles contained in p-th molecule and $\mathbf{r}_i^{(p)}$ is the position of the i-th particle in p-th molecule.

The calculation of the interaction term $\hat{W}(\Gamma)$ is done by introducing several assumptions. The first assumption is that $\hat{W}(\Gamma)$ depends on Γ only through the segment number density $\hat{\phi}(\mathbf{r};\Gamma)$ as:

$$\hat{W}(\Gamma) = W[\hat{\phi}(\mathbf{r};\Gamma)], \tag{4}$$

where $W[\hat{\phi}(\mathbf{r};\Gamma)]$ means that W is a functional of $\hat{\phi}(\mathbf{r};\Gamma)$. Using the assumption of eqn (4) together with the definition of the δ-functional

$$\delta[\hat{\phi}(\mathbf{r};\Gamma) - \phi(\mathbf{r})] = \int D\{w(\mathbf{r})\} \exp[i\int w(\mathbf{r})\{\hat{\phi}(\mathbf{r};\Gamma) - \phi(\mathbf{r})\}\mathrm{d}\mathbf{r}], \tag{5}$$

the partition function of the system, in eqn (2), can be rewritten as:

$$Z = \frac{1}{M!}\int D\{\phi(\mathbf{r})\}\int D\{w(\mathbf{r})\}\exp\left\{-\beta\left[-\frac{M}{\beta}\ln z + W[\phi(\mathbf{r})\right] - \frac{1}{i\beta}\int w(\mathbf{r})\phi(\mathbf{r})\mathrm{d}\mathbf{r}\right]\right\}, \tag{6}$$

where z is the single molecule partition function in an external field and $w(\mathbf{r})$ is a conjugate field of $\phi(\mathbf{r})$ which appeared in the Fourier representation of the δ-functional, and is a complex field.

The mean field approximation, in terms of partition function, is obtained by replacing the integrals over $w(\mathbf{r})$ and $\phi(\mathbf{r})$ in eqn (6) with a Gaussian integral around the most probable state that minimizes the argument of the exponential function on the right-hand side of eqn (6) (so-called saddle point approximation).

The minimization conditions obtained by functional derivatives are:

$$\begin{cases} V(\mathbf{r}) \equiv \dfrac{1}{i\beta} w(\mathbf{r}) = \dfrac{\delta w[\phi(\mathbf{r})]}{\delta \phi(\mathbf{r})} \\ \phi(\mathbf{r}) = -\dfrac{M}{\beta z} \dfrac{\delta z}{\delta V(\mathbf{r})} = \left\langle \hat{\phi}(\mathbf{r}; \Gamma) \right\rangle \end{cases}, \tag{7}$$

where $\phi(\mathbf{r})$ is the coarse-grained density at position $\mathbf{r}$ and $V(\mathbf{r})$ is the external potential conjugate to $\phi(\mathbf{r})$ which is a real field.

In terms of eqn (7), it is possible to obtain an expression for the external potential acting on each particle. Next, we assume that the density dependent interaction potential W, where each component species is specified by the index K, has the following form:

$$W[\{\phi_{\mathrm{K}}(\mathbf{r})\}] = \int \mathrm{d}\mathbf{r} \left(\frac{k_{\mathrm{B}}T}{2} \sum_{\mathrm{KK}'} \chi_{\mathrm{KK}'} \phi_{\mathrm{K}}(\mathbf{r}) \phi_{\mathrm{K}'}(\mathbf{r}) + \frac{1}{2\kappa} \left(\sum_{\mathrm{K}} \phi_{\mathrm{K}}(\mathbf{r}) - 1 \right)^2 \right), \tag{8}$$

where $\phi_{\mathrm{K}}(\mathbf{r})$ is the coarse-grained density of the species K at position $\mathbf{r}$ and $\chi_{\mathrm{KK}'}$ are the mean field parameters for the interaction of a particle of type K with the density fields due to particles of type K′. Here we redefined $\phi_{\mathrm{K}}(\mathbf{r})$ as the number density of the species K normalized by the total average number density of the particles. This change in the definition of $\phi_{\mathrm{K}}(\mathbf{r})$ only affects the scale of the conjugate field $V(\mathbf{r})$.

The second term of the integrand on the right-hand side of eqn (8) is the relaxed incompressibility condition, where κ is the compressibility that is assumed to be sufficiently small (for the systems considered in this paper the value of $1/\kappa$ is 10 kJ mol^{-1}).[36] Then, the corresponding mean field potential is:

$$V_{\mathrm{K}}(\mathbf{r}) = \frac{\delta W[\{\phi_{\mathrm{K}}(\mathbf{r})\}]}{\delta \phi_{\mathrm{K}}(\mathbf{r})} = k_{\mathrm{B}}T \sum_{\mathrm{K}'} \chi_{\mathrm{KK}'} \phi_{\mathrm{K}'}(\mathbf{r}) + \frac{1}{\kappa} \left(\sum_{\mathrm{K}} \phi_{\mathrm{K}}(\mathbf{r}) - 1 \right). \tag{9}$$

In the case of a mixture of two components A and B as an example, the mean field potential acting on a particle of type A at position $\mathbf{r}$ is given by:

$$V_{\mathrm{A}}(\mathbf{r}) = k_{\mathrm{B}}T[\chi_{\mathrm{AA}}\phi_{\mathrm{A}}(\mathbf{r}) + \chi_{\mathrm{AB}}\phi_{\mathrm{B}}(\mathbf{r})] + \frac{1}{\kappa}(\phi_{\mathrm{A}}(\mathbf{r}) + \phi_{\mathrm{B}}(\mathbf{r}) - 1). \tag{10}$$

Thus, the force acting on the particle A at position $\mathbf{r}$ imposed by the interaction with the density field is

$$F_{\mathrm{A}}(\mathbf{r}) = -\frac{\partial V_{\mathrm{A}}(\mathbf{r})}{\partial \mathbf{r}} = -k_{\mathrm{B}}T \left(\chi_{\mathrm{AA}} \frac{\partial \phi_{\mathrm{A}}(\mathbf{r})}{\partial \mathbf{r}} + \chi_{\mathrm{AB}} \frac{\partial \phi_{\mathrm{B}}(\mathbf{r})}{\partial \mathbf{r}} \right) - \frac{1}{\kappa} \left(\frac{\partial \phi_{\mathrm{A}}(\mathbf{r})}{\partial \mathbf{r}} + \frac{\partial \phi_{\mathrm{B}}(\mathbf{r})}{\partial \mathbf{r}} \right). \tag{11}$$

The main advantage of the hybrid MD-SCF scheme is that the most computationally expensive part of the MD simulations, the calculation of the non-bonded forces, is replaced by the evaluation of forces between single particles with external potentials. In order to connect particle and field models, for the proposed hybrid MD-SCF scheme, it is necessary to obtain a smooth coarse-grained density function directly from the particle position Γ. Let us denote this procedure as

$$\bar{S}\{\hat{\phi}(\mathbf{r};\Gamma)\} = \phi(\mathbf{r}), \tag{12}$$

where $\bar{S}$ is a symbolic name of the mapping from the particle positions to the coarse-grained density $\phi(\mathbf{r})$. This density field is obtained by dividing the simulation box into several sub-cells. Then, according to the position of each particle inside a cell, a fraction of the particle is assigned to each vertex of the cell. In order to explain such procedure, a two-dimensional case is schematized in Fig. 1A.

As shown in Fig. 1B, the fraction of a particle assigned to a given lattice point is proportional to the area of a rectangle shown in the figure. According to the procedure described above, the size of the cell l is a spatial parameter defining the extent of density coarse-graining. The larger the value of l is, more particles will be included in each cell and coarser is the calculated density. Once the coarse-grained density has been calculated from particle positions, the spatial derivatives of the density fields can be evaluated. The iteration algorithm used in the MD-SCF approach is as follows: according to the initial configurations of the system (at time t_0), the starting value of the coarse-grained density is obtained and density gradients at the particle positions are calculated by linear interpolation. Then, from the density gradients, forces acting on the particles at position $\mathbf{r}$ due to the interaction with the density fields are computed according to eqn (11). The total force acting on the particles will be the sum of the intramolecular forces (bonds, angles, *etc.* calculated as in classical MD simulations) and the forces due to the interactions of particles with density fields. After the force calculation, a new configuration is obtained by integration of the equation of motion.

It is worth noting that, for these models the use of the mean field does not correspond to a truly field-based method or just particle–field coexistence. The density field remains a close function of particle coordinates, and is not an independent variable in the free energy functional. According to the instantaneous field approximation discussed by Daoulas *et al.* in the framework of SCMF Monte Carlo simulations,[34] it is possible to tune a time interval to update the density field without loss of accuracy. The main assumption is that the field, as a collective

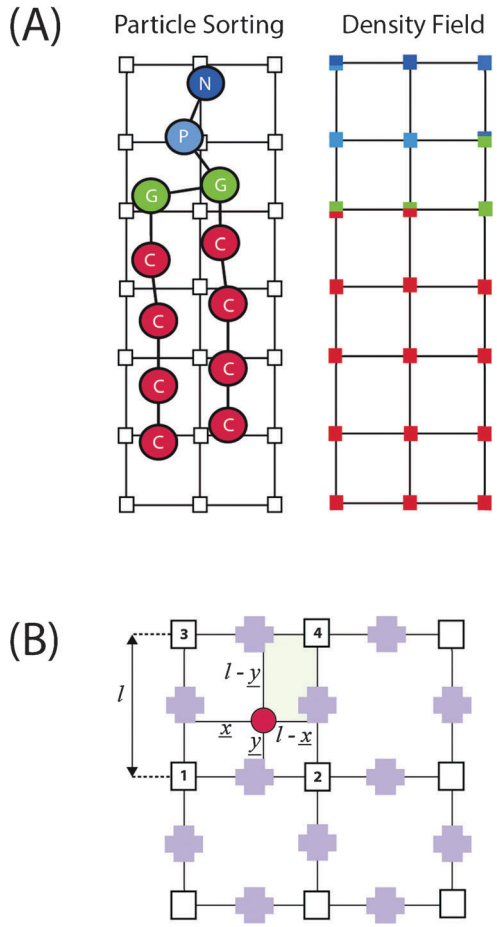

Fig. 1 (A) Assignment of coarse-grained density to the lattice points for a phospholipid. (B) Criterion for assignment to a particle fraction to lattice points.

variable with respect to particle coordinates, undergoes a slow change with respect to particle displacements in one or more timesteps. The optimal value of updating frequency (Δt_{update}) depends on the resolution of the density (*i.e.* the size of the sub-cell where the particles are grouped), the system nature and its conditions. For the systems considered here and reported in ref. 36–40 we found that the value of Δt_{update} starting from 600 to lower values of time steps gives enough accurate results.

Simulation details

Simulations reported here have been performed using the parallelized version of the OCCAM code.[41]

All simulations have been performed using a velocity Verlet algorithm with a time step of 0.03 ps in the NVT ensemble by keeping the temperature constant at 325 K using an Andersen thermostat with a collision frequency of 7 ps^{-1}. The calculations of the fields have been performed using a grid resolution of 0.705 nm and an update frequency (Δt_{update}) of 300 steps.

Models and parameters

The coarse-grained models adopted in this study for lipids have been extensively described and validated in two previous papers.[38,39] These models suitable for modelling biomembranes have been recently reviewed.[31] For the models used in this work for Pluronics, intramolecular bonded interactions, bond and angle potentials have been taken from the ones reported in ref. 25 while non-bonded interactions are described using a field theoretic approach.

The parametrization of the MD-SCF models suitable for Pluronics has been done considering different reference systems. Models of PEO and PPO chains have been developed considering effective particles, centered at the oxygen atoms, each of them grouping the atoms of one repeating unit. The mapping scheme adopted in this work is depicted in Fig. 2. The scheme can be considered as 3 : 1 mapping for PEO and 4 : 1 mapping for PPO, *i.e.* three (for the EO unit) and four (for the PO unit) non-hydrogen atoms are grouped into one bead.

Bonds are described by a harmonic potential of the form:

$$V_{\text{bond}}(l) = \tfrac{1}{2}K_{\text{bond}}(l - l_0)^2, \qquad (13)$$

where l_0 is the equilibrium bond length and K_{bond} is the force constant. Parameters for all bond types are reported in Table 1.

The stiffness of the chains is also taken into account by a bending potential $V_{\text{angle}}(\theta)$ that depends on the cosine of the angle θ between two successive bonds.

$$V_{\text{angle}}(\theta) = \tfrac{1}{2}K_{\text{angle}}\{\cos(\theta) - \cos(\theta_0)\}^2, \qquad (14)$$

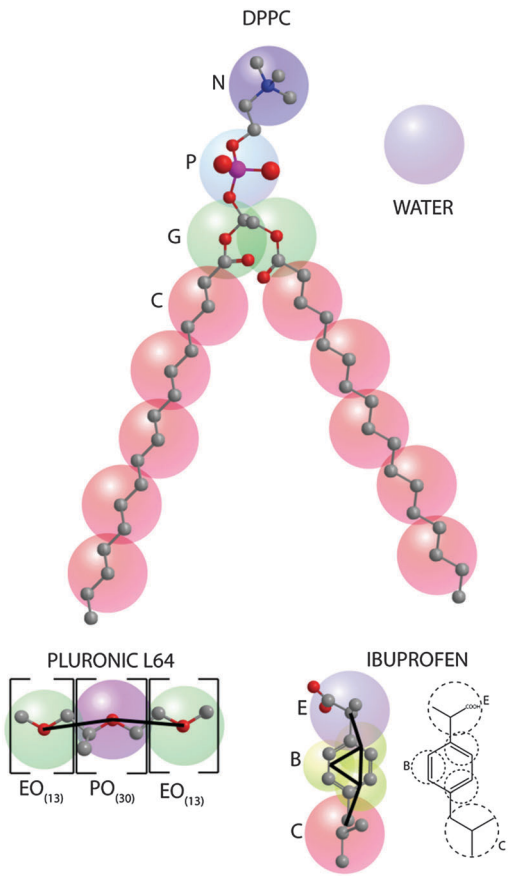

Fig. 2 Mapping scheme adopted for the models considered in this paper.

Table 1 Force field bond parameters

Bond type	l_0 (nm)	K_{bond} (kJ mol^{-1} nm^{-2})
N–P	0.470	1250.0
P–G	0.470	1250.0
G–G	0.370	1250.0
G–C	0.470	1250.0
C–C[a]	0.470	1250.0
EO–EO	0.280	8000.0
PO–PO	0.280	5000.0
EO–PO	0.280	6500.0
E–B	0.310	7500.0
B–B	0.270	8000.0
B–C	0.310	7500.0

[a] These parameters have been used also for the trimer model.

Table 2 Force field angle parameters

Angle type	θ (deg)	K_θ (kJ mol^{-1})
P–G–G	120.0	25.0
P–G–C	180.0	25.0
G–C–C	180.0	25.0
C–C–C	180.0	25.0
EO–EO–EO	155.0	40.0
EO–PO–PO	140.0	40.0
EO–EO–PO[a]	140.0	30.0
PO–PO–PO	140.0	40.0
E–B–B	150.0	50.0
B–B–B	120.0	50.0
B–B–C	150.0	50.0

[a] These parameters have been used also for the trimer model.

where K_{angle} is the force constant and θ_0 is the equilibrium bond angle. Parameters adopted for all angle types are reported in Table 2.

According to eqn (9), in order to calculate the MD-SCF potential, several mean field parameters $\chi_{KK'}$ between particles of type K with the density field due to particles of type K′ are needed. In Table 3 the set of $\chi_{KK'}$ parameters used in this study are reported. Models of lipid bilayers have been fully validated in ref. 38 and 39. Mean field $\chi_{KK'}$ parameters for the interaction of ethylene oxide (EO) and propylene oxide (PO) repeating units with water and lipid bilayers have been tuned to reproduce several reference data from atomistic simulations.[23] Further details of the parametrization are given in the following sections.

Table 3 Particle–field interaction matrix. χ_{AB}·RT (kJ mol^{-1}) for systems I–III

	N	P	G	C	Water	EO	PO
N	0.00	−1.50	6.30	9.0	−8.10	−5.25	2.60
P	−1.50	0.00	4.50	13.50	−3.60	−0.75	7.55
G	6.30	4.50	0.00	6.30	4.50	5.00	0.00
C[a]	9.00	13.50	6.30	0.00	33.75	7.80	−1.60
Water	−8.10	−3.60	4.50	33.75	0.00	1.50	4.60
EO[b]	−5.25	−0.75	5.00	7.89	1.50	0.00	16.00
PO	2.60	7.55	0.00	−1.60	4.60	16.00	0.00

[a] The same parameters have been used for the particle of type B of IBU molecules. [b] The same parameters for the particle of type E of IBU molecules.

Table 4 Particle–field interaction matrix. χ_{AB}·RT (kJ mol^{-1}) for system IV

λ	N	P	G	C	Water	EO	PO
1.00	9.00	13.50	6.30	0.00	33.75	7.80	−1.60
0.90	7.28	11.79	6.12	3.37	30.37	7.22	−0.98
0.80	5.57	10.80	5.94	7.75	27.00	6.64	−0.36
0.60	2.14	6.66	5.58	13.50	20.25	5.84	0.88
0.50	0.43	4.95	5.40	16.87	16.87	4.90	1.50
0.20	−4.70	−0.18	4.86	27.00	6.75	3.16	3.61
0.16	−5.39	−0.86	4.79	28.35	5.40	2.93	3.61

Results and discussion

L64 single chains and micelles in water

Mean field interaction parameters ($\chi_{KK'}$ of eqn (9), given in Table 3) of EO and PO beads and water have been tuned to reproduce the behavior of the gyration radius with respect to the chain length obtained from atomistic simulations. An initial set of parameters for the interaction of EO and PO with water ($\chi_{PEO,W} \times RT = 2.1$ and $\chi_{PPO,W} \times RT = 3.4$ kJ mol^{-1}) has been derived from a_{ij} parameters used in Dissipative Particle Dynamics (DPD) models reported by Cao *et al.*[42] and using the linear relationship introduced by Groot and Warren[43] connecting χ and a ($\chi = 0.286\ \Delta a$). These initial values have been adjusted to the values reported in Table 3 to reproduce chain dimensions obtained from atomistic simulations of PEO and

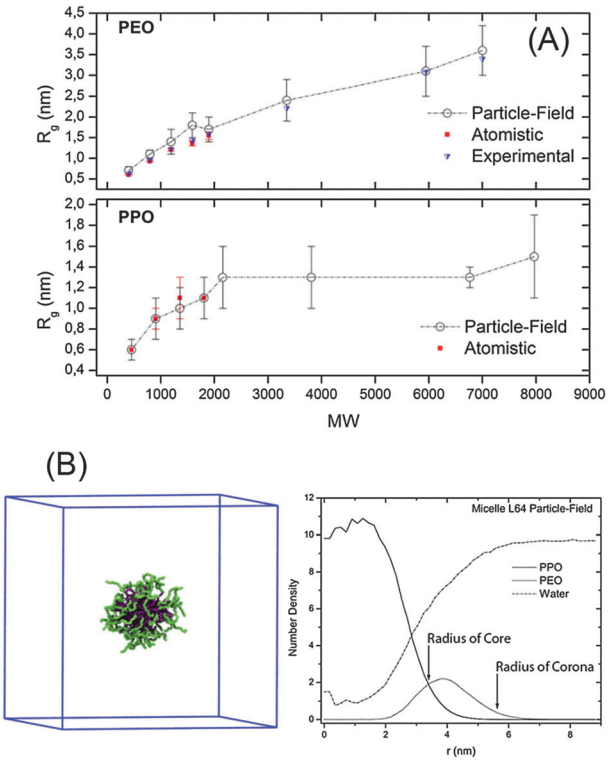

Fig. 3 (A) Radius of gyration *vs.* molecular weight for PEO (upper) and PPO (bottom) chains in water. In the plots values obtained from atomistic simulations (red squares), experiments (blue triangles) and coarse-grained MD-SCF models (empty circles) are compared. (B) Radial density profile calculated for a L64 micelle (system I) after 4.5 μs of MD-SCF simulation. Arrows indicate experimental values of core and corona radii.

PPO single chains in water. In Fig. 3A values of radius of gyration as for different molecular weights (MW) calculated using MD simulations of the atomistic model and MD-SCF simulations of coarse-grained models of PEO and PPO are reported.

A validation of the proposed models for assembled chains has been done considering the size and the stability of micelles. In particular, the Pluronic L64 represented by the formula $(EO)_{13}$–$(PO)_{30}$–$(EO)_{13}$ has been considered. In Fig. 3B, together with a snapshot of simulated system I of Table 6, the radial density profiles calculated for a L64 micelle having 38 block copolymer chains (corresponding to the experimental aggregation number) are reported. Experimental values of core and corona radius[44] are indicated by arrows in the plot. The radial density profiles of PO and EO blocks calculated from a simulation of system I (2.5 wt% of L64 in water) compare well with the experimental values of core and corona radii obtained under the same conditions.[44]

The critical micelle concentration (CMC) of the L64 model has been investigated considering the stability of the system as a function of L64 concentration. In particular, fractions of assembled L64 chains have been calculated for systems at different concentrations (Table 5). In Fig. 4 the fraction of assembled L64 chains compared with the experimental value of the CMC is reported. A good agreement with the value of 0.344 mM reported by Alexandridis[45] has been obtained. Further validations on micelle behavior (aggregation number) are reported in the ESI.‡ The Pluronic model reported here gives the correct reproduction of the occurrence of micellar and non-micellar phases for Pluronics L62 and L64 as a function of water concentration. In particular, the proposed models are able to correctly describe the different morphologies (such as hexagonal micellar, lamellar and complex interconnected structures) that have been found experimentally.[40]

Table 5 Composition of systems used for the CMC calculation[a]

	Composition				
System	No. L64	No. water	No. particles	mM	Box size (nm)
A	19	223 264	224 328	1.122	30 × 30 × 30
B	9	223 824	224 328	0.532	30 × 30 × 30
C	6	223 992	224 328	0.354	30 × 30 × 30
D	5	224 048	224 328	0.295	30 × 30 × 30
E	4	224 104	224 328	0.236	30 × 30 × 30

[a] The experimental value of CMC reported by Alexandridis[45] is 0.344 mM at 313 K.

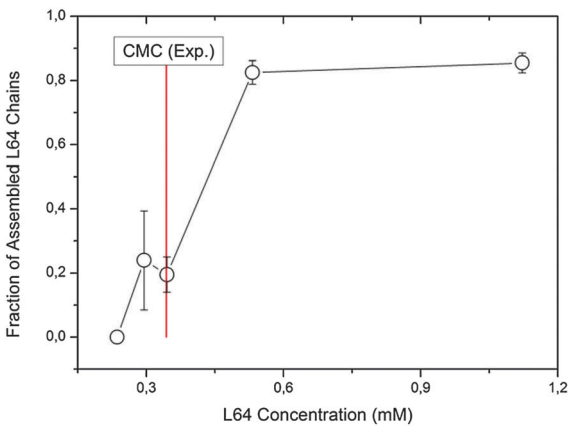

Fig. 4 Fraction of assembled L64 chains at different concentrations, corresponding to the systems described in Table 5. Chains are counted as assembled if the number of neighboring chains is different from zero. The number of neighbors is calculated on the basis of a cut off criterion (1 nm) on the shorter distance between PO units of two different L64 chains. Each point in the plot corresponds to an average obtained from the last 100 ns of each simulation. The time behavior of the fraction of assembled chains for all the five systems is reported in the ESI.‡

Micelles in contact with the DPPC bilayer

The parametrization of the interaction parameters $\chi_{KK'}$ between EO and PO beads with phospholipids (Table 3) has been based on the reproduction of density profiles from reference atomistic simulations of PEO and PPO oligomers in contact with lipid bilayers.[24] An initial set of χ for EO and PO interactions with heads and tails of lipids has been obtained from a systematic DPD study of Groot on polymer–surfactant systems. In particular, values of set 1 (according to the notation of ref. 43) for EO/lipid head and EO/lipid tail and intermediate values between sets 6 and 7 for PO/lipid head and PO/lipid tail have been chosen. Further slight adjustments of parameters have been done to better reproduce reference partial density profiles obtained from atomistic simulations. Density profiles and description of systems used for the parametrization are reported in ESI.‡

According to the experimental data the diameter of the micelle is around 12 nm.[44] For this reason, in order to avoid large finite size effects, in the simulations reported here, a box of size 2.5 times larger than the micelle diameter in the x and y directions (30 nm) and 2.8 times in the z direction (34 nm) has been employed. This implies simulations of quite large-scale systems having more than 250 000 particles (see Table 6).

In Fig. 5A several snapshots of the MD simulation of system II made of one Pluronic L64 micelle in contact with a DPPC lipid bilayer are presented (water beads are not shown for clarity). The simulation performed on the μs scale reveals that the behavior of the polymeric micelle is strongly influenced by the presence of a lipid bilayer. In particular, from the beginning of the simulation chains are released from the micelle to the water phase and starting from about 1 μs insertion of Pluronic triblock chains inside the bilayer can be observed. This behavior is in agreement with the experimental one reported by Pembouong *et al.*[46] In particular, the results obtained using ^{1}H-NMR spectroscopy and spin labeled probes suggest the release of L64 chains inside dodecylphosphocholine (DPC) and DPPC micelles.

Simulation snapshots show that chains attach to the lipid bilayer by inserting the hydrophobic segment made of PO beads into the hydrophobic portion of the bilayer. In Fig. 5C details of an inserted L64 chain of system II are provided. In agreement with the findings of Firestone *et al.*,[47,48] chains are inserted partially inside the bilayer with the PPO block, while

Table 6 Simulated systems

	Composition (no. of molecules)						
Systems	L64	Water	DPPC	Embedded molecule	Particle no.	Box size (nm)	Simulated time (μs)
I	38	222 200	0	0	224 328	30 × 30 × 30	6
II	38	222 200	2812	0	258 072	30 × 30 × 34	5
III[a]	38	222 200	2812	5	258 097	30 × 30 × 34	13
IV-A[b]	38	222 200	2812	8	258 096	30 × 30 × 34	5
IV-B[b]	38	222 200	2812	8	258 096	30 × 30 × 34	5
IV-C[b]	38	222 200	2812	8	258 096	30 × 30 × 34	6
IV-D[b]	38	222 200	2812	8	258 096	30 × 30 × 34	21
IV-E[b]	38	222 200	2812	8	258 096	30 × 30 × 34	15
IV-F[b]	38	222 200	2812	8	258 096	30 × 30 × 34	18
IV-G[b]	38	222 200	2812	8	258 096	30 × 30 × 34	18

[a] Embedded molecules used for this system are Ibuprofen. [b] System IV having embedded trimers of increasing hydrophobicity λ ranging from 0.16 (IV-A) to 1 (IV-G).

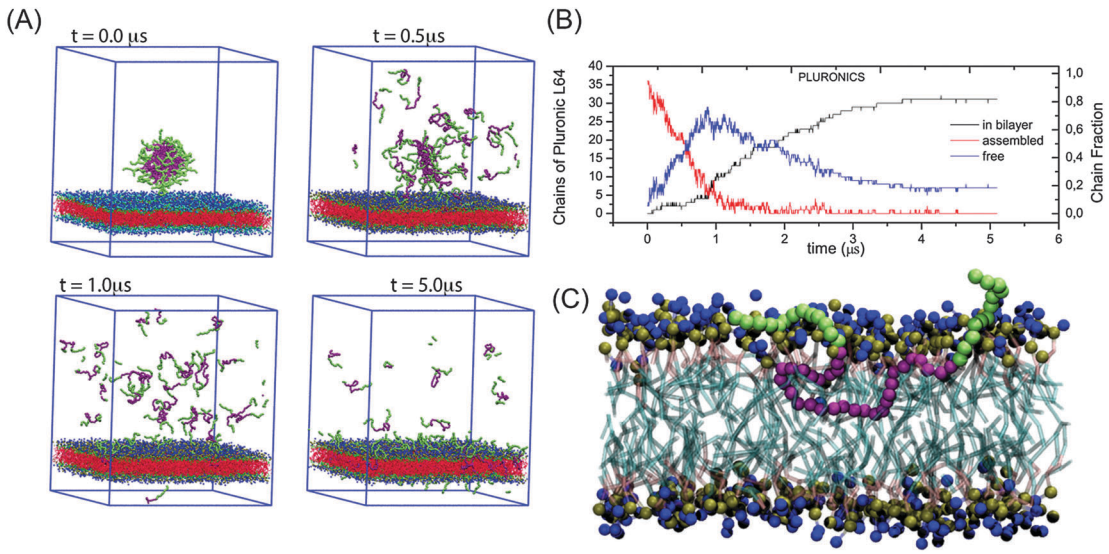

Fig. 5 (A) Snapshots of system II (258 072 coarse-grained beads corresponding to ~3 000 000 of atoms) having a L64 micelle in contact with the DPPC lipid bilayer (water beads are omitted for clarity). (B) Time behavior of L64 chains assembled as micelle (red curve), inside the lipid bilayer (black curve) and in water (blue curve). L64 chains, for a given configuration, are counted as inside the bilayer if at least one PO bead is located between the average heights of upper and lower lipid layers. The remaining chains are counted as free or assembled according to the number of neighboring chains (zero neighbor free chains, at least one neighbor assembled chains). The number of neighbors is calculated on the basis of a cut off value (1 nm) on the shortest distance between PO units of two different L64 chains. (C) Details of insertion of a Pluronic L64 chain inside the phospholipid bilayer. The green beads correspond to EO units, while the purple beads correspond to PO units. The aliphatic chains of phospholipids are shown in transparency. The head groups of DPPC are shown.

the PEO blocks point toward the water phase from the same side of the lipid bilayer. The chain release process continues until the micelle dissolves in the water phase. This behavior can be ascribed to an effective concentration of L64 in the water phase lower than the CMC due to the subtraction of polymer chains from the micellar assembly and from water caused by the insertion inside the lipid bilayer. From the plot of Fig. 5B it is clear that in about 3 μs the L64 chains are unassembled with a fraction of 0.2 present as free chains and the remaining L64 chains inserted inside the lipid bilayer.

Usually, for coarse-grained models the dynamics is faster than the corresponding atomistic ones. This happens because there is a reduced effective bead friction due to smaller energy barriers and/or smoother energy landscapes. In order to connect the results with less coarse models (atomistic or CG but based on particle–particle potentials) or with experiments it is necessary to derive a scaling factor for the time.[49] Methods to match time scales can be applied to quantitatively understand and predict dynamics of several systems by coarse-grained models using a comparison between dynamical properties calculated at coarse-grained and atomistic levels. One possible way is the comparison between diffusion coefficients calculated from the coarse-grained models and atomistic simulations. In the present case, from the comparison of diffusion coefficients a factor of about 15 can be obtained.[38] This simple comparison can give just an idea because the complication in soft matter systems is the multitude of energy barriers of similar height and a common problem is that usually all barriers are not lowered in the exact same way.

In order to better define the scaling factor for the process of chain insertion into a lipid bilayer, a closer timescale connection

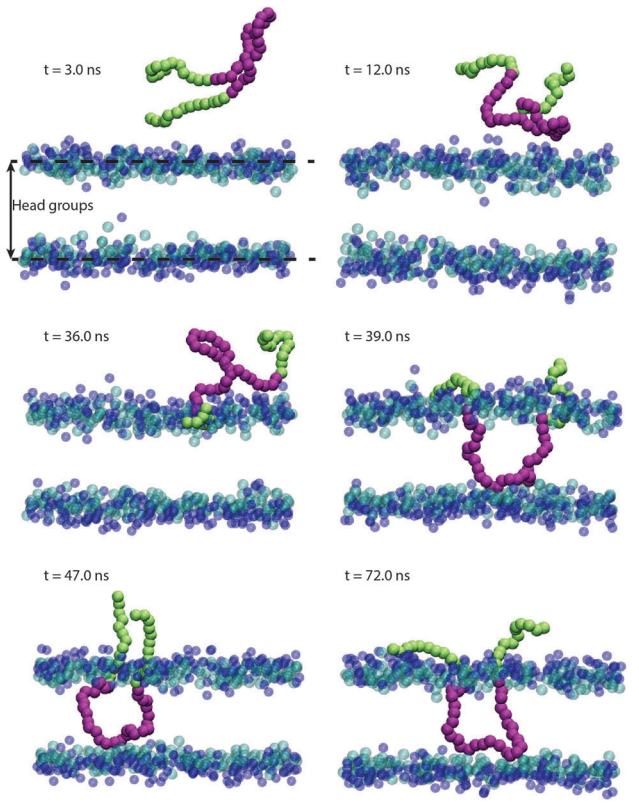

Fig. 6 Snapshots of the single L64 chain insertion process for an MD-SCF simulation. The insertion of the PPO hydrophobic block is observed starting from 39 ns. The L64 chain after insertion shows the hydrophobic block inside the aliphatic region of the phospholipid bilayer, while PEO blocks point toward the water phase from the same side.

can be made comparing the time needed for the insertion of a single chain using MD-SCF and MD using traditional models based on Lennard-Jones pair potentials. Ideally, the exchange process of L64 chains between the micelle and the lipid bilayer, reported in the present paper, can be divided into three elementary processes. In particular, we can consider three processes: Pluronic chain detachment from the micelle, chain diffusion in water, and chain insertion into the lipid bilayer. Reasonably, the diffusion process is the slowest one and it governs the rate of the observed process. In order to prove this, we performed three independent simulations similar to the one reported in Fig. 6. In particular, we analyzed the velocity of L64 chain insertion from the time behavior of the z component (perpendicular to the bilayer plane) for the distance between the geometric center of the PPO block and the hydrophobic sector of the lipid bilayer. According to this analysis, chain insertion is fast (takes about 8–10 ns) and it shows similar velocities for both particle–particle and particle–field simulations. More details of this are reported in the ESI.‡

We can reasonably conclude that the slowest process governing the chain exchange between the micelle and the bilayer is the diffusion of L64 chains. In this way, a reasonable estimate of the order of magnitude of the scaling factor, for the observed process, could be the ratio of diffusion coefficients of particle–particle to particle–field simulations (a factor of 15).

This feature allows us to fully observe on the scale of our simulations the exchange of polymer chains between the micelle and the bilayer and the dissolution process of the micelle in the presence of the lipid bilayer. Furthermore, equilibrium values of the distribution of L64 chains inserted into the bilayer and in the water phase can be reached.

In the absence of a lipid bilayer, we found that the micelle is stable. In particular, in Fig. 7A, several snapshots of the MD simulation for 6 μs of a system having an L64 micelle in water (system I) are presented. Furthermore, the time behavior of radius of gyration of the micelle in water is reported in Fig. 7B. Differently from system II the micelle is stable and an exchange of few chains between the micelle and the water phase is only observed.

In Fig. 8A we show snapshots of system III, which is analogous to system II, but having four molecules of ibuprofen (IBU) encapsulated into the hydrophobic core of the micelle. In Fig. 2 the mapping scheme used for an IBU molecule together with its chemical structure is presented. In particular, the isopropyl group has been modeled using a bead of type C, the benzene ring using three beads of type B (having the same χ parameters as those of beads of type C) and the carboxylic group (COOH) using a bead of type E (having the same χ parameters as those of beads of type EO). Further details of intramolecular interactions (bonds and angles) of beads of types B and E are provided in Tables 1 and 2. The number of IBU molecules corresponds to 0.25 wt% with respect to the quantity of L64. This value, as reported by Foster *et al.*, is consistent with the aggregation number of 38 chains.[50]

Similarly to the previously described system II, after about 1 μs (Fig. 8B) the insertion of triblock chains into the bilayer takes place, but differently from the previous system II, although a reduction of micelle size is observed (Fig. 8C), the micellar assembly is not dissolved. In particular, after 5 μs the micellar aggregate reaches its equilibrium size, and starting from 5 up to 9 μs only a slow repartition between chains in water and inside the bilayer occurs. After 9 μs up to the end of simulation (about 5 μs) the system remains in an equilibrium state.

From these results it is clear that the hydrophobic nature of the encapsulated molecule influences the stability of the micellar assembly in the presence of a lipid bilayer. Small-angle neutron scattering and pulsed-field gradient stimulated-echo nuclear magnetic resonance (NMR) have shown that addition of hydrophobic molecules to solutions of Pluronics and water changes the micellar structure. In particular, high hydrophobic molecule concentrations favor micellization, leading to an increase of aggregation numbers, fraction of polymers micellized, and the core radius of the micelle.[50] This behavior can be ascribed to the hydrophobic nature of the molecule encapsulated inside the micelle and the resulting favorable interactions with the micelle core.

In order to validate the results based on a single simulation, we reported and compared the results of three different independent simulations for system III described above. In particular, comparison between the behavior of block averages of the different simulations and the instantaneous time behavior

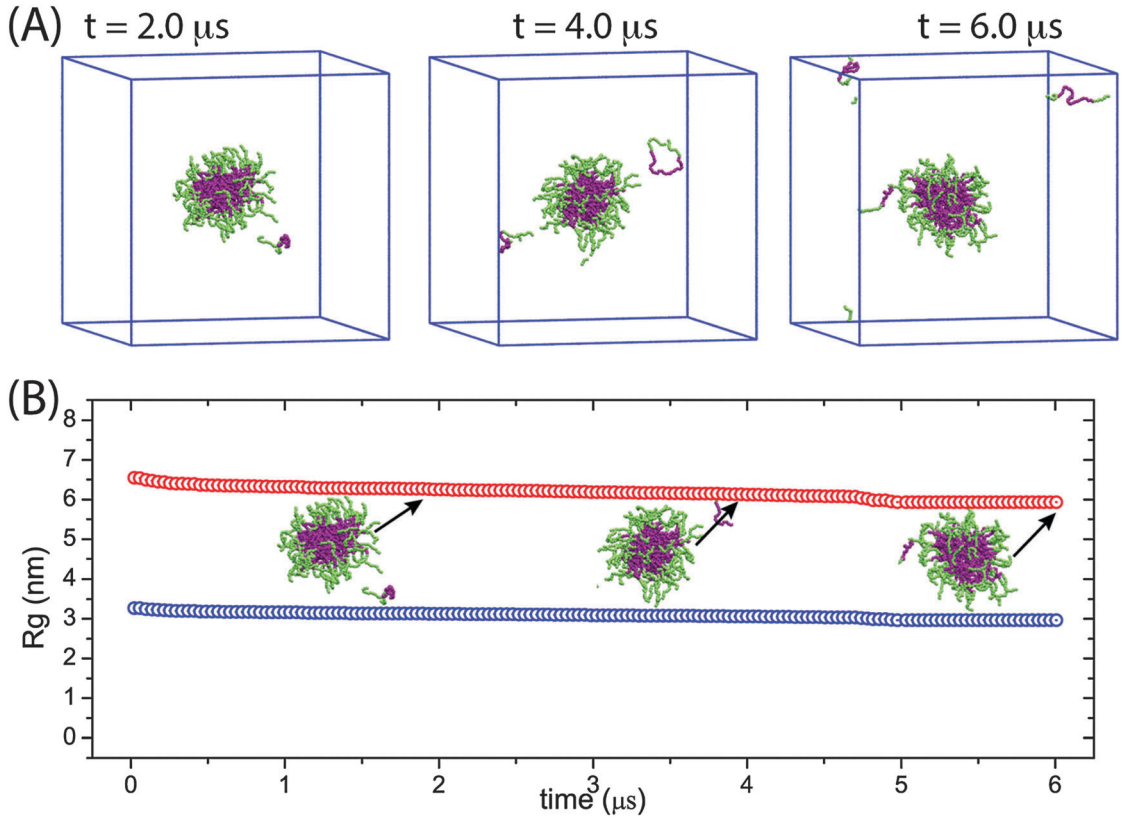

Fig. 7 (A) Snapshots of system I having an L64 micelle in water (the beads of water are omitted for clarity). (B) Time behaviour of radius of gyration of L64 micelle in water. The red curve corresponds to the total radius of gyration of micelle while the blue curve corresponds to the radius of gyration of the hydrophobic core. Snapshots of some configurations of the L64 micelle are shown at different times.

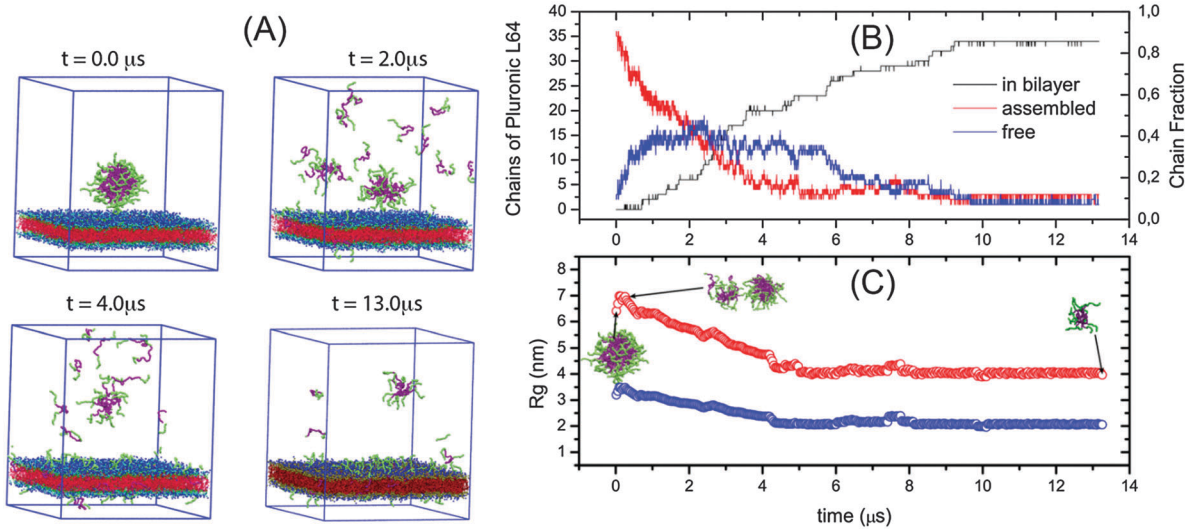

Fig. 8 (A) Snapshots of system III (258 072 coarse-grained beads corresponding to ~3 000 000 of atoms) having an L64 micelle in contact with the DPPC lipid bilayer (water beads are omitted for clarity). (B) Time behavior of L64 chains assembled as the micelle (red curve), inside the lipid bilayer (black curve) and in water (blue curve). For a complete definition of assembled, free and inside bilayer chains the reader can refer to the caption of Fig. 4. (C) Time behavior of radius of gyration of L64 micelle with ibuprofen molecules embedded in the hydrophobic core. Red curve corresponds to the total radius of gyration of the micelle while the blue curve corresponds to the radius of gyration of the hydrophobic core. Snapshots of relevant configuration of L64 micelle are shown at different times.

of the three different states of Pluronic chains (free, assembled and inserted into the bilayer) shows similar features. In particular, the main behavior in all three cases is very similar and at equilibrium the chain distributions converge to very close values. Due to their similarity, we expect close behaviors in all considered systems. More information

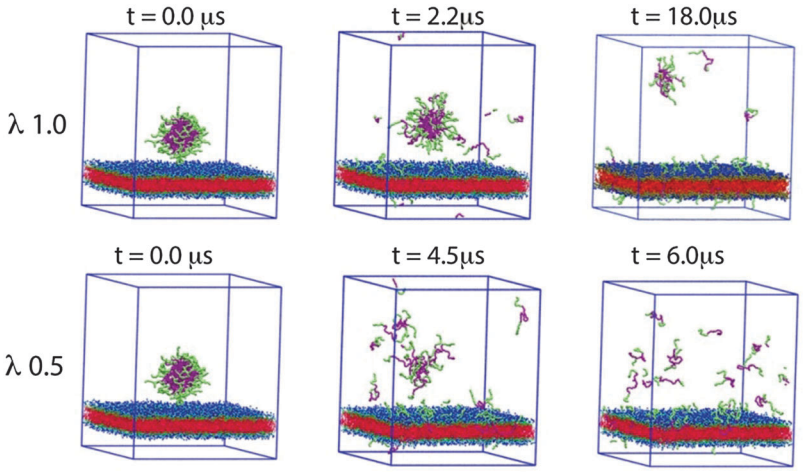

Fig. 9 Snapshots of systems IV (258 072 coarse-grained beads corresponding to ~3 000 000 of atoms) at different values of λ having an L64 micelle in contact with the DPPC lipid bilayer.

about this validation including plots and their comparison is provided in the ESI.‡

In our simulations the presence of the lipid bilayer changes the micelle aggregation state. In particular, in the absence of IBU molecules, 80% of L64 chains are inserted inside the DPPC bilayer. This causes a drop of L64 concentration in the water phase and then the destabilization of micellar aggregates. In contrast, in the presence of hydrophobic IBU molecules, L64 chains are still assembled. This behavior shows a complex interplay of drug–micelle core and L64–bilayer interactions modulating the structural modifications of both the micelle and the bilayer. The main effect of the drug molecule seems to be related to its hydrophobicity.

With this in mind, further simulations aimed to study systematically this effect have been performed. In particular, trimers of increasing hydrophobicity have been included in the hydrophobic core of the L64 micelles. The number of trimers included in the micelle core is 8; this choice has been made to keep the number of particles similar to that in system III in which 5 IBU molecules (represented 5 by coarse-grained beads) have been included. The hydrophobicity of the trimers has been varied by changing linearly the χ parameters from the values assigned to the most hydrophobic particles (type C of lipid molecules) to those ones of water using a single parameter λ. In this way $\lambda = 1$ corresponds to a particle of type C and $\lambda = 0$ to a particle with the properties of water. For the intermediate cases, a linear combination has been used for all parameters. Simulations have been performed for seven different systems (IV-A to IV-G) having values of λ (0.16, 0.2, 0.5, 0.6, 0.8, 0.9, 1.0). In Table 4 the corresponding χ parameters for interaction between the beads of the trimers and the fields corresponding to other particle types are reported.

In Fig. 9 representative snapshots for some of these systems have been presented. For trimers having λ larger than 0.5 the micelles are stable during MD simulations. After 10 s the micelle aggregate does not change and it still remains stable up to the end of simulation. The behavior observed for values of λ lower than 0.5 is very similar to the one obtained for an "empty" micelle. For lower values of λ (from 0.16 to 0.2) after about 10 ns all the inserted molecules diffuse out from the micelle and are stably present in the water phase. This is not surprising because the properties of the beads forming trimers at these values of λ are very close to water. For values larger than 0.5 all the included trimers are stable inside the micelle from the beginning to the end of the simulation. In Fig. 10 the time behavior of L64 chain distributions inside the bilayer, assembled and free are reported for all systems with λ larger than 0.5 (0.6, 0.8, 0.9, 1.0). The plots of other systems are given in the ESI.‡ We observe that the higher the hydrophobicity, the slower the chain release process from the micelle to the water phase. In particular, for the systems at λ = 0.16 and 0.20 the micelle dissolution process takes 1 and 2 μs, respectively. Differently, the system having trimers with λ = 0.5 take longer

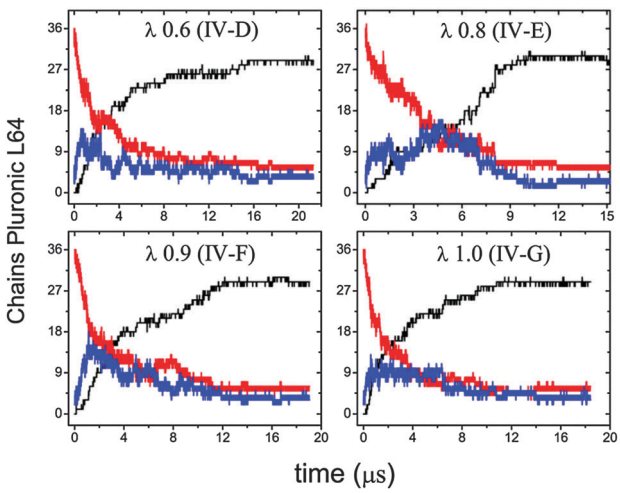

Fig. 10 Time behaviour of systems IV D–G of L64 chains assembled as micelle (red curve), inside the bilayer (black), and in water (blue). For a complete definition of assembled, free and inside bilayer chains the reader can refer to the caption of Fig. 5.

(between 4 and 5 μs) to reach the equilibrium. Micelles including trimers of larger hydrophobicity (λ from 0.6 to 1.0) take 8–12 μs, depending on the system, to reach equilibrium. After that time the micelles still remain stable and a slow process of chain repartition between water and lipid bilayer occurs.

It is worth noting that an increase of hydrophobicity corresponds to an abrupt increase of the number of assembled chains. In particular, when going from λ = 0.5 to λ = 0.6, an increase in the micelle radius of about nine times can be obtained.

Moreover, we observe that the number of assembled chains, for systems in which the micellar aggregate is present, does not change significantly (Fig. 11B). A similar behavior is found for shape and size of the micellar aggregate, for which the radial density profiles have been calculated. In particular, for system III, and systems IV(D)–IV(G), the radial density profiles of the assembled chains in equilibrium together with IBU or trimer molecules (Fig. 12) have been calculated. The radial density of chains when embedding IBU or the trimer molecules does not change significantly. In particular, for both hydrophilic EO blocks and hydrophobic PO blocks, only slight differences have been found (Fig. 12A and B). As for the radial density of IBU and trimer molecules, from the comparison of Fig. 12C, we found that the distribution of IBU or trimer molecules inside the PO core is almost the same as that for all systems, but showing a slightly larger preference for the center of the micelle for both IBU molecules and trimers having λ = 1.

In Fig. 13 some of the density profiles of the lipid bilayer have been reported. In particular we compared the density profiles of system II (without IBU), system III (with IBU molecules inside the micelle) and system IV-G (with trimer molecules having λ = 1.0).

Such profiles have been calculated after each system reached the equilibrium state. From the plots we observe that the lipid bilayers do not show sensible differences in the profile. The heads and tails of the lipids are distributed very close to each other and seem to be insensitive to the hydrophobicity. For the distribution of Pluronic chains inside the lipid bilayer we observe the same behavior (in the ESI‡ all the density profiles of other systems are provided).

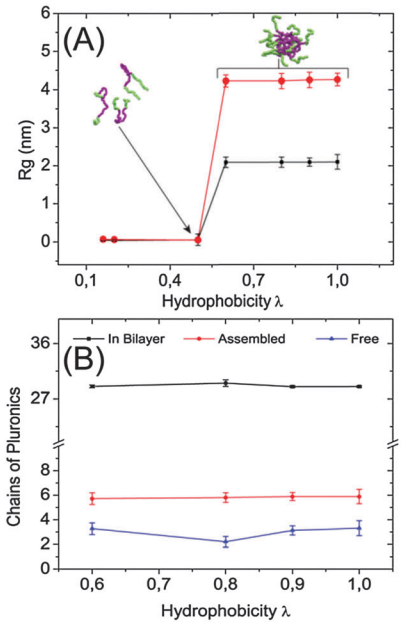

Fig. 11 (A) Behavior of the radius of gyration of L64 micelle at different values of λ. Total radius (red curve) and hydrophobic core radius (black curve). (B) Behavior of assembled (red curve), in bilayer (black curve) and free (blue curve) L64 chains as a function of hydrophobicity (λ) of encapsulated trimers.

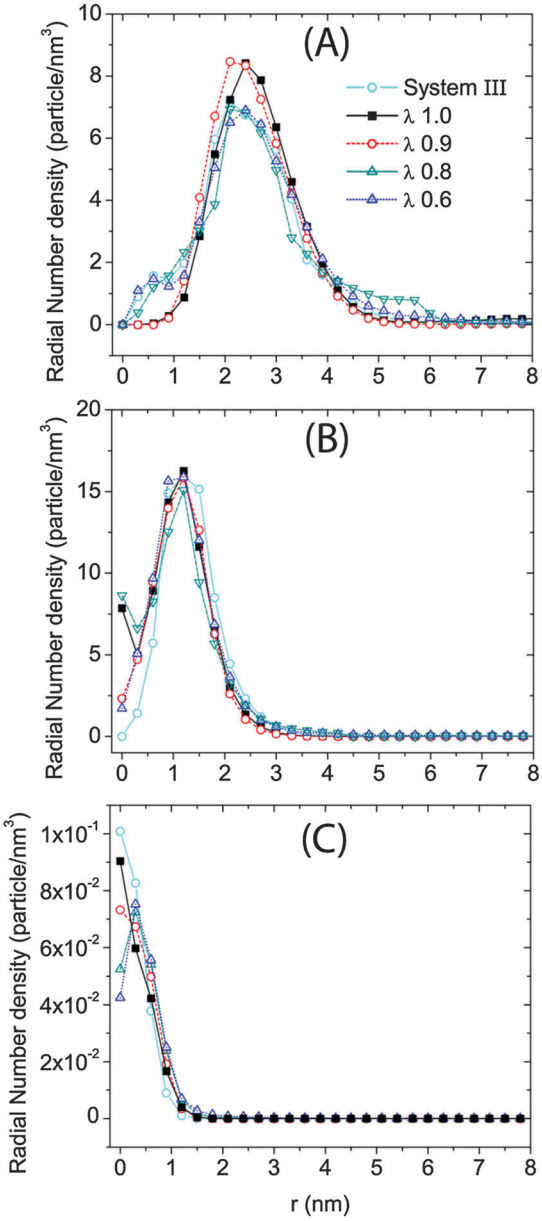

Fig. 12 Radial density profile of: (A) EO blocks, (B) PO block, and (C) IBU and trimer embedded molecules. Each profile is calculated with respect to the centre of the mass of IBU or trimer molecules. The profiles have been calculated from the data during the last 500.0 ns of the equilibrium state of each system.

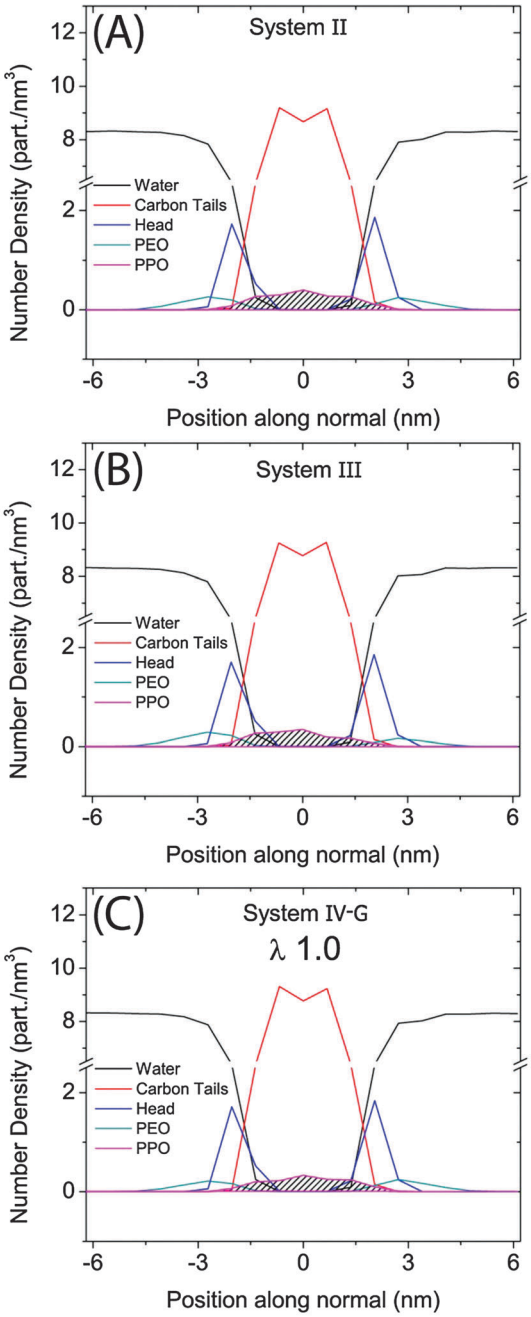

Fig. 13 Number density profiles calculated for: (A) system II, (B) system III and (C) system IV-G with λ = 1.0. The density profiles have been calculated for the data during the last 500.0 ns of the equilibrium state of each system.

Conclusions

The development and validation of coarse-grained models of Pluronics that are able to describe micellar assemblies and their interactions with phospholipids have been reported. Molecular dynamics simulations of large-scale coarse-grained models (typically ~260 000 coarse-grained beads corresponding to ~3 000 000 of atoms) of Pluronic L64 block copolymer micelles interacting with lipid bilayers suitable to reach time (μs) and length (nm) scales relevant to the self-assembly phenomena for several systems have been reported. Simulations show, in agreement with several previous experiments, the release of triblock chains from the micelle inside the bilayer. This release changes the size of the micelles. The presence of a drug molecule inside the hydrophobic core of the micelle has a strong influence on this process. In particular, the micelle stability is a result of a complex interplay of drug–core and block-*co*-polymer–bilayer interactions modulating the structures of both the micelle and the bilayer. An interesting finding is that the micelle size shows an abrupt increase in the very narrow range of encapsulated molecule hydrophobicity. Changes in aggregate size and structure are critical to determine the mechanism of drug delivery from micellar structures. According to the paradigm of the EPR effect, the understanding of the physico-chemical mechanism of the drug vector size and the important role of drug–micelle interactions in it are fundamental to improve the design of systems for cancer therapy. The models presented in this study are not generic, but still very close to atomistic ones and are able to represent specific molecular architectures. This important feature opens the way to a detailed understanding of the molecular mechanisms underlying the drug delivery processes.

Acknowledgements

G.M. and D.R. thank Deutschen Forschungsgemeinschaft (DFG) for funding the framework of the project "The study of detailed mechanism of polymer–biological membrane interactions using computer simulation" (RO 3571/3-1). G.M. thanks MIUR (PRIN2008 and FIRB "RETE ITAL-NANONET") for financial support. Moreover, G.M. thanks the European Soft Matter Infrastructure (ESMI) and Forschungszentrum Juelich team for the HPC facilities (www. fz-juelich.de).

Notes and references

1 R. Duncan and R. Gaspar, *Mol. Pharmaceutics*, 2011, **8**, 2101–2141.
2 R. Duncan, *Curr. Opin. Biotechnol.*, 2011, **22**, 492–501.
3 R. Duncan, *Nat. Rev. Drug Discovery*, 2003, **2**, 347.
4 R. Duncan, *Nat. Rev. Cancer*, 2006, **6**, 688.
5 G. Pasut and F. M. Varonese, *Adv. Drug Delivery Rev.*, 2009, **61**, 1177.
6 Y. Matsumura, *Adv. Drug Delivery Rev.*, 2008, **60**, 899.
7 Y. Matsumura and K. Kataoka, *Cancer Sci.*, 2009, **100**, 572.
8 D. Farrel, K. Ptak, N. J. Panaro and P. Grodzinski, *Pharm. Res.*, 2011, **28**, 273.
9 T. M. Allen, *Nat. Rev. Drug Discovery*, 2002, **2**, 750–763.
10 V. P. Torchilin, *Nat. Rev. Drug Discovery*, 2005, **4**, 145.
11 W. C. Zamboni, *Clin. Cancer Res.*, 2005, **11**, 8230.
12 K. K. Upadhyay, H. G. Agrawal, C. Upadhyay, C. Schatz, J. F. Le Meins, A. Misra and S. Lecommandoux, *Crit. Rev. Ther. Drug Carrier Syst.*, 2009, **26**, 157.

13 A. B. Kabanov, E. V. Batrakova and V. Y. Alakhov, *Adv. Drug Delivery Rev.*, 2002, **54**, 759.
14 Y. Matsumura and H. Maeda, *Cancer Res.*, 1986, **6**, 6387.
15 A. B. Kabanov, V. P. Chekhonin, V. Alakhov, E. V. Batrakova, A. S. Lebedev, N. S. Melik-Nubarov, S. A. Arzhakov, A. V. Levashov, G. V. Morozov and E. S. Severin, *FEBS Lett.*, 1989, **258**, 343.
16 V. Y. Alakhov and A. V. Kabanov, *Expert Opin. Invest. Drugs*, 1998, **7**, 1453–1473.
17 A. A. Exner, T. M. Krupka, K. Sherrer and J. M. Teets, *J. Controlled Release*, 2005, **106**, 188.
18 M. Hans, K. Shimoni, D. Danino, S. J. Siegel and A. Lowman, *Biomacromolecules*, 2005, **6**, 2708.
19 V. Alakhov, E. Klinski, S. Li, G. Pietrzynski, A. Venne, E. Batrakova, T. Bronitch and A. Kabanov, *Colloids Surf., B*, 1999, **16**, 113–134.
20 S. Pal, G. Milano and D. Roccatano, *J. Phys. Chem. B*, 2006, **110**, 26170–26179.
21 S. Nawaz, M. Redhead, G. Mantovani, C. Alexander, C. Bosquillon and P. Carbone, *Soft Matter*, 2012, **8**, 6744–6754.
22 M. Redhead, G. Mantovani, S. Nawaz, P. Carbone, D. C. Gorecki, C. Alexander and C. Bosquillon, *Pharm. Res.*, 2012, **29**, 1908–1918.
23 S. Samanta, S. Hezaveh, G. Milano and D. Roccatano, *J. Phys. Chem. B*, 2012, **116**, 9286.
24 S. Samanta, S. Hezaveh, G. Milano and D. Roccatano, *J. Phys. Chem. B*, 2012, **116**, 5141–5151.
25 S. Hezaveh, S. Samanta, A. De Nicola, G. Milano and D. Roccatano, *J. Phys. Chem. B*, 2012, **116**, 14333–14345.
26 P. F. J. Fuchs, H. S. Hansen, P. H. Huenenberger and B. A. C. Horta, *J. Chem. Theory Comput.*, 2012, **8**, 3943–3963.
27 S. Hezaveh, S. Samanta, G. Milano and D. Roccatano, *J. Chem. Phys.*, 2012, **136**, 124901.
28 S. Hezaveh, S. Samanta, G. Milano and D. Roccatano, *J. Chem. Phys.*, 2011, **135**, 16450.
29 K. M. Langner and G. J. A. Sevink, *Soft Matter*, 2012, **8**, 5102–5118.
30 M. Mueller, K. Katasov and M. Schick, *Phys. Rep.*, 2006, **434**, 113–176.
31 M. Giuseppe, K. Toshihiro and N. Antonio De, *Phys. Biol.*, 2013, **10**, 045007.
32 M. Hömberg and M. Müller, *J. Chem. Phys.*, 2010, **132**, 155104–155118.
33 G. J. A. Sevink, M. Charlaganov and J. G. E. M. Fraaije, *Soft Matter*, 2013, **9**, 2816–2831.
34 K. C. Daoulas and M. Müller, *J. Chem. Phys.*, 2006, **125**, 184904.
35 K. C. Daoulas, M. Müller, J. J. de Pablo, P. F. Nealey and G. D. Smith, *Soft Matter*, 2006, **2**, 573–583.
36 G. Milano and T. Kawakatsu, *J. Chem. Phys.*, 2009, **130**, 214106.
37 G. Milano and T. Kawakatsu, *J. Chem. Phys.*, 2010, **133**, 214102.
38 A. De Nicola, Y. Zhao, T. Kawakatsu, D. Roccatano and G. Milano, *J. Chem. Theory Comput.*, 2011, **7**, 2947–2962.
39 A. De Nicola, Y. Zhao, T. Kawakatsu, D. Roccatano and G. Milano, *Theor. Chem. Acc.*, 2012, **131**, 1167.
40 A. De Nicola, G. Milano and T. Kawakatsu, *Macromol. Chem. Phys.*, 2013, **214**, 1940–1950.
41 Y. Zhao, A. De Nicola, T. Kawakatsu and G. Milano, *J. Comput. Chem.*, 2012, **33**, 868–880.
42 X. Cao, G. Xu, Y. Li and Z. Zhang, *J. Phys. Chem. A*, 2005, **109**, 10418–10423.
43 R. D. Groot and P. B. Warren, *J. Chem. Phys.*, 1997, **107**, 4423–4435.
44 L. Yang, P. Alexandridis, D. C. Steytler, M. J. Kositza and J. F. Holzwarth, *Langmuir*, 2000, **16**, 8555–8561.
45 P. Alexandridis, J. F. Holzwarth and T. A. Hatton, *Macromolecules*, 1994, **27**, 2414–2425.
46 G. Pembouong, N. Morellet, T. Kral, M. Hof, D. Scherman, M.-F. Bureau and N. Mignet, *J. Controlled Release*, 2011, **151**, 57–64.
47 M. A. Firestone and S. Seifert, *Biomacromolecules*, 2005, **6**, 2678–2687.
48 M. A. Firestone, A. C. Wolf and S. Seifert, *Biomacromolecules*, 2003, **4**, 1539–1549.
49 D. Fritz, K. Koschke, V. A. Harmandaris, N. F. van der Vegt and K. Kremer, *Phys. Chem. Chem. Phys.*, 2011, **13**, 10412–10420.
50 B. Foster, T. Cosgrove and B. Hammouda, *Langmuir*, 2009, **25**, 6760–6766.